Supplemental Material: Doping fingerprints of spin and lattice fluctuations in moiré superlattice systems

Niklas Witt,[1, 2, ∗] José M. Pizarro,[1, 3, †] Jan Berges,[1] Takuya Nomoto,[4] Ryotaro Arita,[4, 5] and Tim O. Wehling[1, 2]

[1]*Institute of Theoretical Physics, Bremen Center for Computational Materials Science,*
and MAPEX Center for Materials and Processes,
University of Bremen, Otto-Hahn-Allee 1, 28359 Bremen, Germany
[2]*I. Institute of Theoretical Physics, University of Hamburg, Notkestraße 9, 22607 Hamburg, Germany*
[3]*Max Planck Institute for the Structure and Dynamics of Matter,*
Luruper Chaussee 149, 22671 Hamburg, Germany
[4]*Department of Applied Physics, The University of Tokyo,*
7-3-1 Hongo, Bunkyo-ku, Tokyo 113-8656, Japan
[5]*RIKEN Center for Emergent Matter Science, 2-1 Hirosawa, Wako, Saitama 351-0198, Japan*

In Section S1 of this Supplemental Material, we give a short description of the low-energy continuum model developed in Ref. [S1] for Γ-valley twisted transition metal dichalcogenides (TMDCs) which we employed here. We show the band structure for all Γ-valley twisted TMDCs, WS_2, MoS_2, and $MoSe_2$, at different twist angles θ. In Section S2, we present the Wannier construction for the two top-most superlattice valence bands in a twist angle range of $1° < \theta < 5°$. In Section S3, we discuss the effect of the long-range Coulomb interactions on the low-energy flat bands in presence of doping in the Hartree approximation. We follow the procedure from Refs. [S2, S3] for magic-angle twisted bilayer graphene (MATBG). Section S4 gives estimations of the of the electronic Coulomb interaction strength, in particular the on-site and nearest-neighbor interaction parameters U and V. In Section S5, we explain the calculations in the fluctuation exchange (FLEX) approximation [S4, S5]. In Section S6, we discuss the nature of magnetic ordering, analyze the momentum dependence of the static spin susceptibility at different dopings δ and temperatures T/t, and show its real space profile. In Section S7, we investigate the leading superconducting order parameter and possible pairing symmetries in the honeycomb Hubbard model at various dopings and temperatures. Section S8 discusses the influence of longer-ranged hopping terms on spin fluctuations and superconductivity. In Section S9 we investigate the influence of non-local electron-phonon coupling as well as dispersive phonon frequencies on the doping dependence of phonon-mediated superconductivity. In Section S10 we provide an estimation of the effective electron-phonon interaction U_{eff} used for the Holstein model calculations in the main text and for the non-local Peierls coupling employed in Section S9.

S1. LOW-ENERGY CONTINUUM MODEL FOR Γ-VALLEY TWISTED TMDCS

We outline here the low-energy continuum model which we used for the description of the moiré valence band structure of Γ-valley twisted TMDCs. The model was introduced in Ref. [S1], from where we outline here the main points. In this continuum model, only the valence antibonding state at the Γ point is considered, which is isolated from other bands by hundreds of meV because of the interlayer coupling. Since the bands around the Γ-point are mainly of transition metal d_{z^2}-character, spin-orbit coupling effects are small and can be neglected. Because of this, the description of these Γ-valley twisted TMDCs is easier than other TMDC systems like homobilayer WSe_2, where the valence band maximum is at the K-point with strong spin-orbit coupling [S6]. The low-energy Hamiltonian of the continuum model can be written as

$$H = -\frac{\hbar^2 k^2}{2m^*} + V_{\mathrm{M}}(\mathbf{r}), \tag{S1}$$

where m^* is the effective mass and $V_{\mathrm{M}}(\mathbf{r})$ is the moiré potential felt by the holes at the valence band maximum in Γ. The moiré potential has the following expression in real space:

$$V_{\mathrm{M}}(\mathbf{r}) = \sum_{s=1}^{3} \sum_{j=1}^{6} V^s e^{i(\mathbf{g}_j^s \cdot \mathbf{r} + \phi^s)}. \tag{S2}$$

Here, s is the s-th shell of six moiré reciprocal lattice vectors $\mathbf{g}_j^s = \mathcal{R}_{(j-1)\pi/3}\mathbf{G}^s$ ($j = 1, \ldots, 6$) with $\mathcal{R}_\alpha$ being the two-dimensional (2D) rotation matrix about an angle α. We choose reciprocal lattice vectors pointing to the s-th

Table S1. Continuum model parameters for Γ-valley twisted TMDCs. a_0 is the lattice constant in Å, m^* is the effective mass in bare electron mass units, and V^s are in meV. Data taken from Ref. [S1].

	WS$_2$	MoS$_2$	MoSe$_2$
a_0	3.18	3.182	3.295
m^*	0.87	0.9	1.17
V^1	33.5	39.45	36.8
V^2	4.0	6.5	8.4
V^3	5.5	10.0	10.2
$\phi^{1,2,3}$	π	π	π

shell as $\mathbf{G}^1 = \mathbf{G}_2^\mathrm{M}$, $\mathbf{G}^2 = \mathbf{G}_1^\mathrm{M} + \mathbf{G}_2^\mathrm{M}$, and $\mathbf{G}^3 = 2\mathbf{G}_2^\mathrm{M}$, where $\mathbf{G}_{1,2}^\mathrm{M}$ span the reciprocal moiré lattice. The phase factors ϕ^s are constrained by the C_{6z} symmetry of the moiré lattice to be either 0 or π.

The continuum model parameters (m^*, V^s, ϕ^s) were obtained from the *ab initio* calculation of the fully relaxed twisted bilayers, and they are given in Table S1 for the different Γ-valley twisted TMDCs, WS$_2$, MoS$_2$, and MoSe$_2$ [S1]. The maximum of the moiré potential of Eq. (S2) felt by the holes in the valence band maximum is found in the AB/BA regions (see Fig. 1B of Ref. [S1]), so that the low-energy physics of the Γ-valley twisted TMDCs is controlled by orbitals sitting in the honeycomb AB/BA regions.

The diagonalization of H is performed in reciprocal space, where the Hamiltonian of Eq. (S1) is given by (see Eq. (1) in the main text)

$$H = -\frac{\hbar^2 |\mathbf{k} + \mathbf{G}|^2}{2m^*}\delta_{\mathbf{G},\mathbf{G}'} + V_\mathrm{M}(\mathbf{G} - \mathbf{G}'). \tag{S3}$$

$\mathbf{k}$ and $\mathbf{G}$ denote moiré crystal momentum and vectors from the moiré reciprocal lattice, respectively. $V_\mathrm{M}(\mathbf{G} - \mathbf{G}')$ is the Fourier transformation of $V_\mathrm{M}(\mathbf{r})$. This Hamiltonian is expanded up to a plane-wave cutoff G_c for a given twist angle θ. In Fig. S1 we show the band structures for Γ-valley twisted TMDCs at twist angles in the range $1° < \theta < 5°$. The zero energy is defined as the top of the valence band. For this twist angle range it is sufficient to use $G_c = 4-5\ G^\mathrm{M}$, where $G^\mathrm{M} = |\mathbf{G}_{1,2}^\mathrm{M}|$.

From the valence band edge, two flat bands emerge which touch at a Dirac point in the corner of the Brillouin zone and at a certain negative energy. We refer to these bands as "flat Dirac bands" for brevity. These bands are well isolated from other higher energy bands for $\theta < 5°$. The bandwidth of the flat Dirac bands continuously increases approximately quadratically with the twist angle.

Another approach to calculate band structures is the derivation of atomistic tight-binding models, which, for instance, has been done in Ref. [S7] for MoS$_2$. This approach yields the same results and reproduces ab-initio calculations consistently.

S2. WANNIER PROJECTION OF FLAT DIRAC BANDS

Based on our observations in the previous section, we construct a tight-binding Hamiltonian for the isolated flat Dirac bands via Wannier projection with one orbital per sublattice site. The AB and BA regions play the role of the A and B sublattice sites in a honeycomb lattice. The eigenstates of the low-energy continuum model are

$$\Phi_\mathbf{k}^\alpha(\mathbf{r}) \equiv |\Phi_\mathbf{k}^\alpha\rangle = \sum_\mathbf{G} c_{\mathbf{kG}}^\alpha e^{i(\mathbf{k}+\mathbf{G})\cdot\mathbf{r}}, \tag{S4}$$

where α is the band index and $c_{\mathbf{kG}}^\alpha$ are the plane-wave coefficients obtained from the diagonalization of the Hamiltonian from Eq. (S3). We set $G_c = 5G^\mathrm{M}$ and use a k-mesh of 15×15. We consider Gaussian functions centered on A and B sites as the trial orbitals $|g_\mathbf{k}^m\rangle$, whose plane-wave expansion coefficients are given by

$$g_{\mathbf{kG}}^m = e^{-(\Delta\mathbf{K})^2/2}e^{-i\mathbf{K}\cdot\mathbf{l}_m}. \tag{S5}$$

Here, $m \in \{\mathrm{A},\mathrm{B}\}$ is the sublattice (orbital) index, $\mathbf{K} = \mathbf{k} + \mathbf{G}$, and $\mathbf{l}_\mathrm{A} = \mathbf{L}_1^\mathrm{M}/3 + 2\mathbf{L}_2^\mathrm{M}/3$ and $\mathbf{l}_\mathrm{B} = 2\mathbf{L}_1^\mathrm{M}/3 + \mathbf{L}_2^\mathrm{M}/3$ are vectors pointing from the moiré unit cell origin to A and B sites, respectively. $\mathbf{L}_{1,2}^\mathrm{M}$ are the moiré lattice vectors, $\lambda^\mathrm{M} = |\mathbf{L}_{1,2}^\mathrm{M}|$, and $\Delta = \lambda^\mathrm{M}/3$ is the extent of the trial orbitals. These trial orbitals are then projected onto the
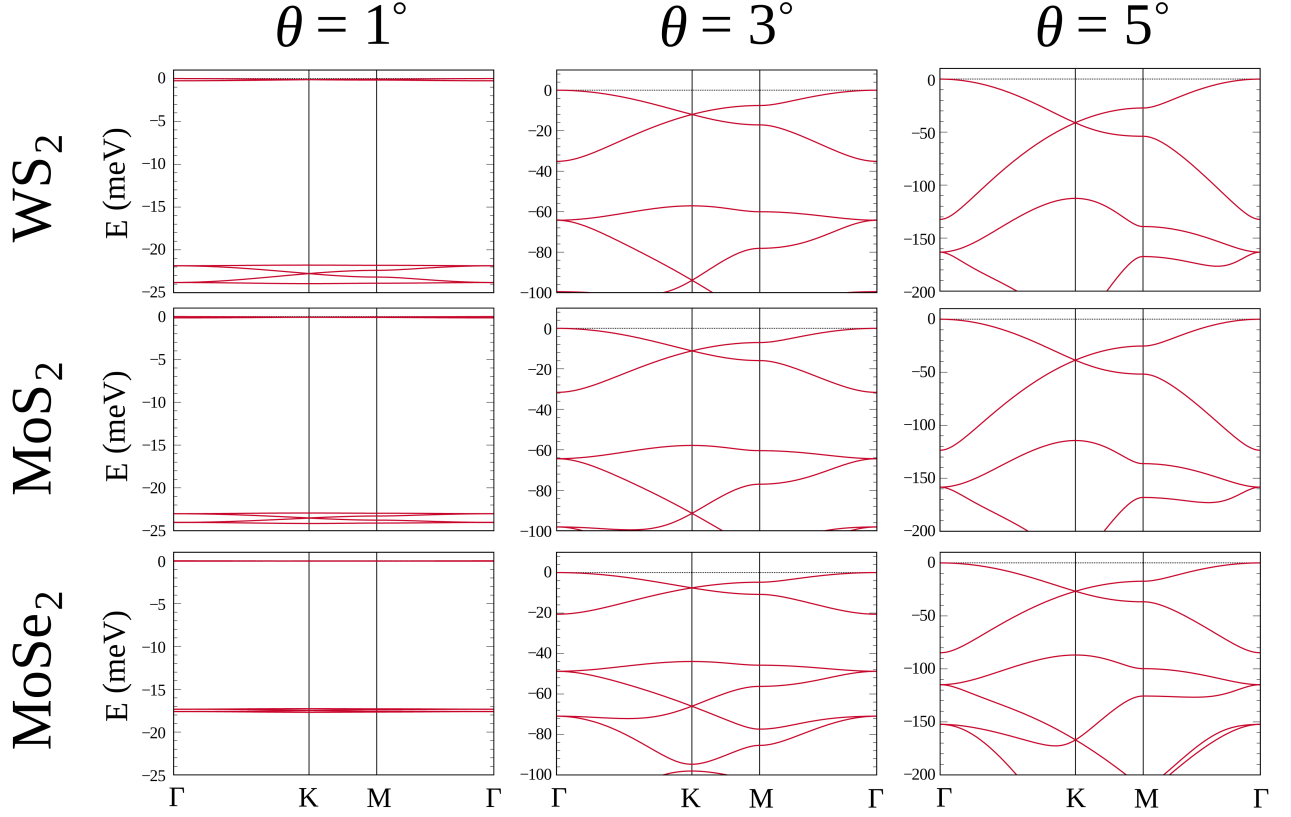
Figure S1. (Color online) Band structures for the Γ-valley twisted TMDCs, WS$_2$ (top row), MoS$_2$ (middle row), and MoSe$_2$ (bottom row). We show the low-energy band evolution for the twist angle range $1° < \theta < 5°$.

eigenstates manifold of the low energy Dirac bands $|\phi_{\mathbf{k}}^m\rangle = \sum_\alpha \langle \Phi_{\mathbf{k}}^\alpha | g_{\mathbf{k}}^m \rangle |\Phi_{\mathbf{k}}^\alpha\rangle$, which yields the corresponding plane-wave expansion coefficients of the state $|\phi_{\mathbf{k}}^m\rangle$ [S8]

$$\phi_{\mathbf{kG}}^m = \sum_\alpha c_{\mathbf{kG}}^\alpha P_{\mathbf{k}}^{\alpha m} . \tag{S6}$$

The projection matrix $P_{\mathbf{k}}^{\alpha m} = \langle \Phi_{\mathbf{k}}^\alpha | g_{\mathbf{k}}^m \rangle \equiv \sum_{\mathbf{G}} (c_{\mathbf{kG}}^\alpha)^\dagger g_{\mathbf{kG}}^m$ allows to calculate the overlap matrix as

$$S_{\mathbf{k}}^{mn} = \langle \phi_{\mathbf{k}}^m | \phi_{\mathbf{k}}^n \rangle = (P_{\mathbf{k}}^\dagger P_{\mathbf{k}})^{mn} . \tag{S7}$$

Eqs. (S6) and (S7) are used to calculate the so-called smooth gauge plane-wave expansion coefficients of the smooth gauge Bloch states $|\tilde{\Phi}_{\mathbf{k}}^m\rangle$

$$\tilde{c}_{\mathbf{kG}}^m = \sum_n \phi_{\mathbf{kG}}^n \cdot (S_{\mathbf{k}}^{-1/2})^{nm} . \tag{S8}$$

The resulting set of well-localized Wannier orbitals can be constructed in real space as

$$\mathcal{W}_{\mathbf{R}m}(\mathbf{r}) = \frac{1}{N_{\mathbf{k}} \sqrt{A_{\mathrm{M}}}} \sum_{\mathbf{k}} \sum_{\mathbf{G}} \tilde{c}_{\mathbf{kG}}^m e^{i\mathbf{K} \cdot (\mathbf{r} - \mathbf{R})} , \tag{S9}$$

where $A_{\mathrm{M}} = \sqrt{3}\lambda^{\mathrm{M}}/2$ is the moiré unit cell size, $\mathbf{r}$ denotes the real space coordinates, and $\mathbf{R}$ describes the Bravais lattice. In Fig. S2(a) we show the real-space probability density $|\mathcal{W}|^2$ for the two Wannier orbitals m from the unit cell at the origin of the Bravais lattice obtained from the flat Dirac bands.

Now, the Hamiltonian in the Wannier orbital basis can be calculated by projecting the continuum Hamiltonian onto the smooth gauge Block states $|\tilde{\Phi}^m\rangle$

$$\tilde{H}_{\mathbf{k}}^{mn} = \langle \tilde{\Phi}_{\mathbf{k}}^m | H | \tilde{\Phi}_{\mathbf{k}}^n \rangle \equiv \sum_{\mathbf{G},\mathbf{G}'} (\tilde{c}_{\mathbf{kG}}^m)^\dagger \tilde{c}_{\mathbf{kG}'}^n H_{\mathbf{kGG}'}, \tag{S10}$$
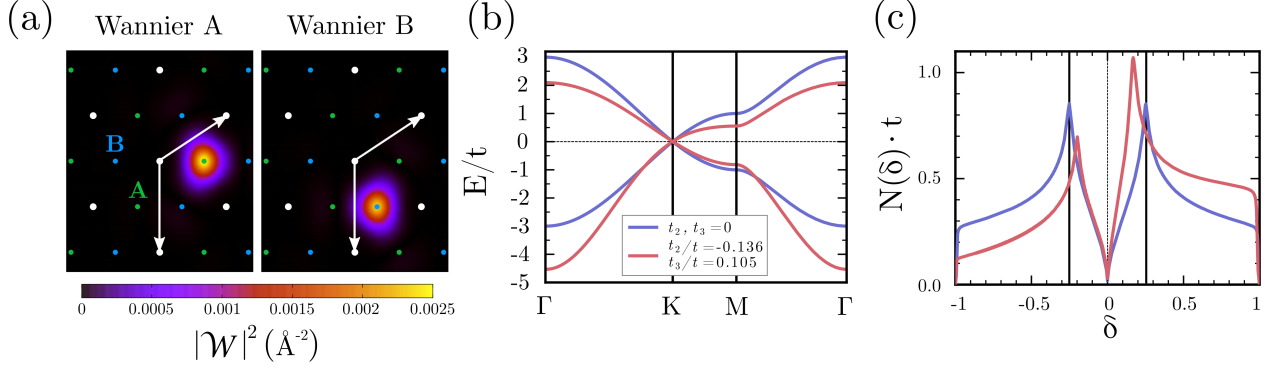
Figure S2. (Color online) Wannier tight-binding model for twisted WS$_2$ at 3.5°. (a) Wannier densities $|\mathcal{W}_m|^2$ for each orbital centered in the sublattices A (green dots) and B (blue dots). White dots denote the Bravais lattice $\mathbf{R}$ and white arrows are the moiré lattice vectors $\mathbf{L}_{1,2}^{\mathrm{M}}$. (b) Band structure and (c) density of states $N(\delta)$ per spin and unit cell of the honeycomb tight-binding model with nearest-neighbor hopping only ($t_2, t_3 = 0$, blue line) and including also longer-ranged hopping terms ($t_2/t_1 = -0.136$, $t_3/t_1 = 0.105$, red line). The doping δ is counted relative to the Dirac point. Van Hove singularities (VHS) appear at the M-points in the Brillouin zone, corresponding to a doping of $\delta = \pm 0.25$ ($\delta \approx -0.2, 0.17$) in the particle-hole symmetric (asymmetric) case.

where $H_{\mathbf{kGG'}}$ are the matrix elements of the Hamiltonian in Eq. (S3). Fourier transformation of Eq. (S10) gives the real space Wannier Hamiltonian $\tilde{H}_{\mathbf{r}}^{mn}$ whose matrix elements m, n are the hopping integrals entering the tight-binding model used in the main text. We find that including up to three nearest-neighbor hoppings is sufficient to describe the band structures found by the continuum model in the twist angle range $1° < \theta < 5°$, as shown in Fig. 1(b) of the main text for WS$_2$ at $\theta = 3.5°$. The angle dependence of the hopping amplitudes is shown in Fig. 1(c) of the main text.

The resulting honeycomb tight-binding model is

$$H_0(\mathbf{k}) = \begin{pmatrix} H_{\mathrm{AA}}(\mathbf{k}) & H_{\mathrm{AB}}(\mathbf{k}) \\ H_{\mathrm{BA}}(\mathbf{k}) & H_{\mathrm{BB}}(\mathbf{k}) \end{pmatrix} \quad \text{with}$$

$$H_{\mathrm{AA}}(\mathbf{k}) = H_{\mathrm{BB}}(\mathbf{k}) = 2t_2 \left[\cos(\mathbf{k} \cdot \mathbf{L}_1^{\mathrm{M}}) + \cos(\mathbf{k} \cdot \mathbf{L}_2^{\mathrm{M}}) + \cos(\mathbf{k} \cdot (\mathbf{L}_1^{\mathrm{M}} + \mathbf{L}_2^{\mathrm{M}})) \right] , \tag{S11}$$

$$H_{\mathrm{AB}}(\mathbf{k}) = H_{\mathrm{BA}}^*(\mathbf{k}) = t_1 \left[1 + e^{i\mathbf{k} \cdot \mathbf{L}_1^{\mathrm{M}}} + e^{i\mathbf{k} \cdot (\mathbf{L}_1^{\mathrm{M}} + \mathbf{L}_2^{\mathrm{M}})} \right] + t_3 \left[2\cos(\mathbf{k} \cdot \mathbf{L}_2^{\mathrm{M}}) e^{i\mathbf{k} \cdot (2\mathbf{L}_1^{\mathrm{M}} + \mathbf{L}_2^{\mathrm{M}})} \right] .$$

The corresponding band structure and density of states (DOS) per spin and unit cell can be found in Figs. S2(b) and (c), respectively. The DOS is shown as a function of doping δ that is counted relative to the Dirac point. We show the third nearest-neighbor hopping model with $t_2/t_1 = -0.136$ and $t_3/t_1 = 0.105$ for WS$_2$ at $\theta = 5°$ using $t \equiv t_1$ as unit of energy. It reveals a slight particle-hole asymmetry around the Dirac point. We also show a simplified model which only accounts for nearest-neighbor hopping and which is particle-hole symmetric. In both cases there are Van Hove singularities (VHS) emerging at the M points of the moiré Brillouin zone.

Since $t_1 \gg t_2, t_3$, the character of the VHS does not change to higher order VHS [S9, S10] and the qualitative physics occurring in the system are not expected to change significantly (c.f. Section S8 for an explicit demonstration). Therefore, we neglect t_2 and t_3 and consider the particle-hole symmetric model with nearest-neighbor hopping $t_1 \equiv t$ only in the main text.

S3. LONG-RANGE COULOMB INTERACTIONS

Several twisted 2D systems are known to show a strong reconstruction of their band structure upon doping caused by the Hartree potential resulting from the long-range Coulomb interaction [S2, S3, S11–S13]. Here, we study the effect of the Hartree potential in Γ-valley twisted TMDCs. We follow the method developed in Ref. [S2]. The Hartree potential contribution to the total Hamiltonian of Eq. (S1) is given by

$$V_{\mathrm{H}}(\mathbf{r}) = \int d^2\mathbf{r}' V_{\mathrm{C}}(\mathbf{r} - \mathbf{r}') \delta\rho(\mathbf{r}'), \tag{S12}$$
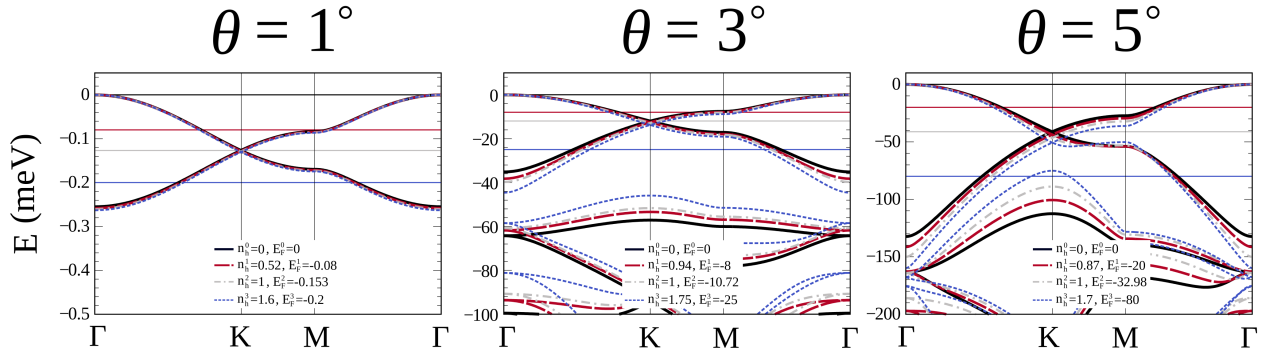
Figure S3. (Color online) Hartree potential effect in the doped band structures of twisted WS$_2$. From left to right, we show results for different twist angles θ. The undoped bands are shown with black solid lines. Band structures corresponding to Fermi levels E_F^i and hole doping n_h^i set between the undoped valence band maximum and the Dirac point (dashed red, $i = 1$), at the Dirac point (dashed gray, $i = 2$), and between the Dirac point and the bottom of the flat Dirac bands (dashed blue, $i = 3$). The solid horizontal lines represent the corresponding Fermi energies. Calculations were performed at $T = 0$.

where $V_\mathrm{C}(\mathbf{r}) = \frac{e^2}{\epsilon|\mathbf{r}|}$ is the Coulomb potential, $\epsilon = 4.5$ is the dielectric constant of the environment as produced by hBN, and $\delta\rho(\mathbf{r})$ is the deviation of the charge density from charge neutrality. $\delta\rho = 0$ corresponds to the undoped continuum model, i.e., when the Fermi level is at the top of the flat Dirac bands. We can then write

$$\delta\rho(\mathbf{r}) = \frac{1}{A_\mathrm{M}} \sum_{\mathbf{G}} \delta\rho(\mathbf{G}) e^{i\mathbf{G}\cdot\mathbf{r}}. \tag{S13}$$

The Fourier components $\delta\rho(\mathbf{G})$ are given by

$$\delta\rho(\mathbf{G}) = -\frac{2}{N_\mathbf{k}} \sum_{\mathbf{k},\mathbf{G}'} \sum_{\alpha'} \left(c_{\mathbf{k}\mathbf{G}'}^{\alpha'}\right)^\dagger c_{\mathbf{k}\mathbf{G}'+\mathbf{G}}^{\alpha'}, \tag{S14}$$

where the sum over α' runs over the unoccupied states in the valence band, so it depends on the doping level E_F, the factor 2 accounts for the spin degeneracy, and the minus sign refers to hole doping. Due to the D_6 symmetry of the lattice, $\delta\rho(\mathbf{G})$ are equally weighted in the same s shell of $\mathbf{g}_j^s$ vectors, so we can write $\delta\rho_s \equiv \delta\rho(\mathbf{g}_j^s)$ for any j. We also checked that it is enough to consider the first and second shells $s = 1, 2$ to correctly address the effect of the Hartree potential. Under these assumptions, we can write the Hartree potential as

$$V_\mathrm{H}(\mathbf{r}) = \sum_s V_0^s \delta\rho_s \sum_j e^{i\mathbf{g}_j^s \cdot \mathbf{r}}, \tag{S15}$$

where $V_0^s = \frac{2\pi e^2}{\epsilon A_\mathrm{M} |\mathbf{G}^s|}$. $\delta\rho_s$ are the amplitudes which define the Hartree potential and have to be determined self-consistently. By Fourier transforming Eq. (S15), we can introduce the Hartree potential in Eq. (S3) and solve the total Hamiltonian $H + V_\mathrm{H}$ in the reciprocal space.

The self-consistent procedure is as follows:

- We consider various doping levels with respect to the top of the valence band n_h (number of holes per spin). Here $n_h = 0$ corresponds to the undoped system, $n_h = 1$ to the hole doping to the Dirac point, and $n_h = 2$ to completely empty flat Dirac bands. We consider n_h^1 between the undoped level and the Dirac point, n_h^2 at the Dirac point, and n_h^3 between the Dirac point and the bottom of the flat Dirac bands. We obtain the plane-wave coefficients $c_{\mathbf{k}\mathbf{G}}^\alpha$ from diagonalizing $H + V_\mathrm{H}$.

- Using Eq. (S14), we calculate the new charges $\delta\rho_s^{\mathrm{new}}$.

- In each iteration step, the self-consistent convergence is checked by $|\delta\rho_s^{\mathrm{old}} - \delta\rho_s^{\mathrm{new}}| < 10^{-6}$. If the convergence criterion is fulfilled, we finish the code and calculate the new and renormalized band structures.

- If the convergence criterion is not fulfilled, then we update $\delta\rho_s$ using a Kerker mixing procedure [S14], where $\delta\rho_s = \delta\rho_s^{\mathrm{old}} + \alpha \frac{G_s^2}{G_s^2 + \beta^2} \left(\delta\rho_s^{\mathrm{new}} - \delta\rho_s^{\mathrm{old}}\right)$. We set $\alpha = 0.1$, $\beta = 0.9$, and $G_s \equiv |\mathbf{G}^s|$. A simple straight mixing is obtained if β is set to a very small value. We find that the charges are usually converged after less than 30 iterations depending on the chosen twist angle θ and the doping level n_h^i.
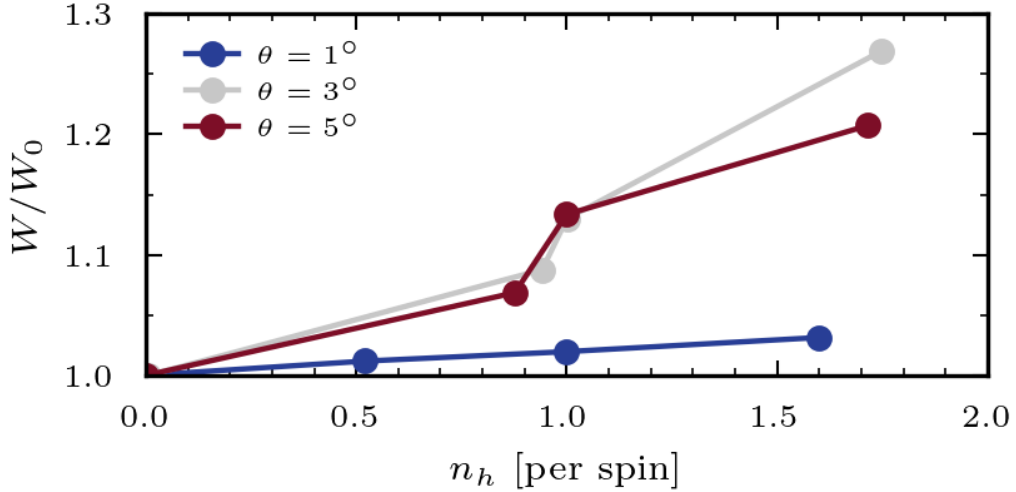
Figure S4. (Color online) Relative change in the bandwidth with respect to the undoped case W/W_0 due to the Hartree potential in twisted WS$_2$. The change is larger for large hole dopings and non-monotonous in terms of the twist angle. The largest relative change for $\theta = 3°$ at $n_h \approx 1.75$ is approximately 27 %.

We show in Fig. S3 the effect of the Hartree potential for WS$_2$ at different twist angles θ and different Fermi energies E_F^i corresponding to respective hole dopings n_h^i. The Hartree potential mainly shifts the bands as a whole and increases the bandwidth. Only for larger twist angles $\theta \geq 5°$ and dopings n_h^3, the flat Dirac bands start to be reconstructed, with the higher energy bands below the flat Dirac bands even being partially filled. This is in contrast to graphene-based systems, where the entangled multiorbital nature of the flat bands facilitate strong renormalization of the bands.

The bandwidth renormalization can be easily visualized when plotting the relative change of the bandwidth with respect to the undoped case W/W_0, see Fig. S4, where the change is larger for larger dopings. The change is non-monotonic when changing the twist angle. From these results, we conclude that $\theta \leq 5°$ is the limit of applicability of our calculations. In any case and for the purpose of our FLEX calculations, we can assume that the doping $\delta = 1 - n_h$ used in the main text occurs between the valence band maximum and the Dirac point, where the bands are essentially unaffected by the Hartree potential.

S4.   ESTIMATION OF THE COULOMB INTERACTION STRENGTH

From the definition of the Wannier orbitals in Eq. (S9), we estimate the value of the screened Coulomb interaction matrix elements $W_{\mathbf{R},mn}$. The local and nearest-neighbor Coulomb interactions can be then calculated as the matrix elements $U \equiv W_{\mathbf{0},AA}$ and $V \equiv W_{\mathbf{0},AB}$. The resulting extended Hubbard model can be mapped onto a local Hubbard model by making the assumption $U^\star = U - V$ [S15]. We estimate the upper and lower bounds by projecting an effective interaction $V_{\text{eff}}(\mathbf{r})$ onto the Wannier functions in two limiting dielectric environment cases: free-standing twisted bilayers, for which the external screening is minimal, and a metallic gate in direct contact with the twisted bilayers, for which the external screening is maximal [S16]. The screened Coulomb interaction matrix is given by

$$W_{\mathbf{R},mn} = \iint d^2\mathbf{r}\, d^2\mathbf{r}'\, V_{\text{eff}}(\mathbf{r} - \mathbf{r}')\rho_{\mathbf{R}m}(\mathbf{r})\rho_{\mathbf{0}n}(\mathbf{r}'), \tag{S16}$$

with $\rho_{\mathbf{R}m}(\mathbf{r}) = |\mathcal{W}_{\mathbf{R}m}(\mathbf{r})|^2$. $V_{\text{eff}}(\mathbf{r})$ is the Coulomb interaction screened by the TMDC bilayer in its undoped state and the dielectric environment. We start from an Ohno potential [S17]

$$V_{\text{Ohno}}(\mathbf{r}) = \frac{e^2}{\sqrt{r^2 + \xi^2}} \tag{S17}$$

that regularizes the bare Coulomb interaction e^2/r at a short wavelength cut-off $\xi = 1$ Å, which is set by the spacial extent of the W d-orbitals. The effect of screening is easily included in reciprocal space, so the effective interaction is
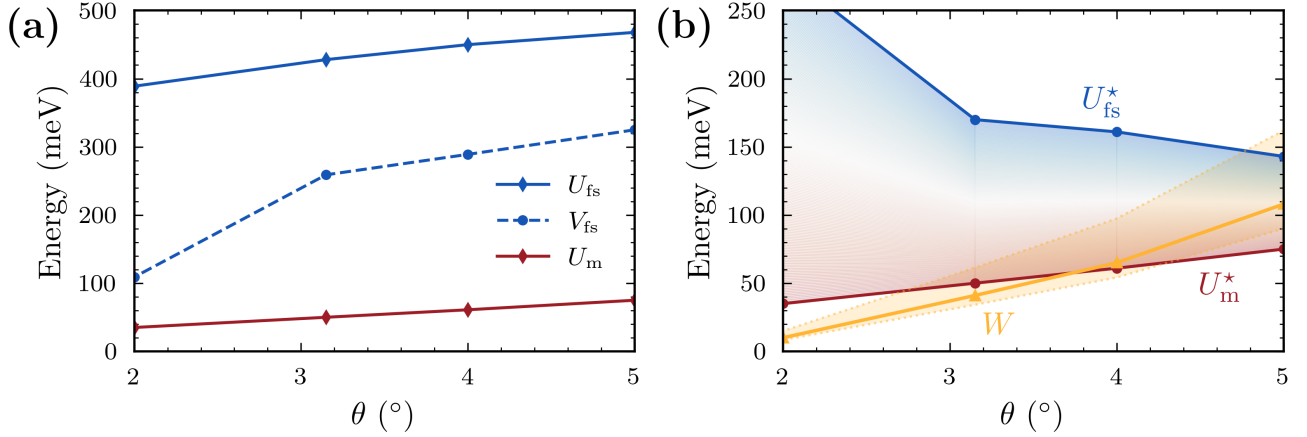
Figure S5. (Color online) Estimated Coulomb interactions in different dielectric environments for WS_2. (a) Local and nearest-neighbor Coulomb interaction U and V in two dielectric environments, free-standing twisted bilayer ('fs', red line) and metallic gate in direct contact with the twisted bilayer ('m', blue line). (b) Effective local Hubbard interactions $U^\star = U - V$ and bandwidth W (orange line). The blue-red shaded region describes the possible values that $U^\star$ can take depending on the dielectric environmental setup. The orange-shaded region indicates interaction values we use in the FLEX calculations ($U^\star/t \sim 5-9$).

$V_{\mathrm{eff}}(\mathbf{r})$ then calculated from the inverse Fourier transformation of

$$V_{\mathrm{eff}}(\mathbf{q}) = \frac{V_{\mathrm{Ohno}}(\mathbf{q})}{\epsilon(\mathbf{q})} = \frac{2\pi e^2}{\epsilon(\mathbf{q})q} e^{-q\xi} , \tag{S18}$$

where $\epsilon(\mathbf{q})$ is the dielectric function that encodes the environmental screening effect. For our two limiting cases, free-standing ('fs') and metal in direct contact ('m'), we use the effective dielectric functions [S16, S18]:

$$\epsilon_{\mathrm{fs}}(\mathbf{q}) = \kappa \frac{1 - \tilde{\kappa} e^{-qh}}{1 + \tilde{\kappa} e^{-qh}} , $$
$$\epsilon_{\mathrm{m}}(\mathbf{q}) = \kappa \coth \frac{qh}{2} . \tag{S19}$$

Here, $\kappa \approx 10$ is the internal screening of the twisted TMDC, $h \approx 13$ Å is the bilayer height [S19, S20], and $\tilde{\kappa} = (\kappa - 1)/(\kappa + 1)$. In Fig. S5(a) we plot the on-site and nearest-neighbor interactions U and V at different twist angles θ for the two limiting cases for WS_2. Since the nearest-neighbor interaction with a metal gate contact V_{m} is on the order of 1 meV, we did not include it in the plot. Fig. S5(b) shows the effective local Hubbard interaction $U^\star$ and the bandwidth W. A realistic value for $U^\star$ in Γ-valley twisted TMDCs will fall inside the shaded regions between the limiting cases $U^\star_{\mathrm{fs}}$ and $U^\star_{\mathrm{m}}$ which depends on the experimental setup and which can be tuned by changing the dielectric environment [S16, S21–S25]. For our FLEX calculations, we use $U^\star/t = 5-9$ (where we assume an effective Hubbard model with $U \equiv U^\star$) which is indicated by an orange-shaded region, since $W \approx 6t$. These interaction values correspond to experimentally accessible interaction strengths in a twist angle range of $3-5°$.

S5. NUMERICAL DETAILS OF FLEX CALCULATIONS

We summarize the calculation steps performed in the FLEX approximation [S4, S5] and give details on the numerical parameters used. In the FLEX approximation, one solves the Dyson equation

$$\hat{G}(k)^{-1} = \hat{G}^0(k)^{-1} - \hat{\Sigma}(k) , \tag{S20}$$

with the dressed (bare) Green function G (G^0), self-energy Σ, and the four-momentum $k = (i\omega_n, \mathbf{k})$. $\mathbf{k}$ is the crystal momentum and $\omega_n = (2n + 1)\pi k_{\mathrm{B}}T$ are the Matsubara frequencies at a temperature T. In case of the single-orbital honeycomb model, all quantities are given by 2×2 matrices in terms of sublattice indices A and B [S26, S27] which is denoted by a hat $G_{\alpha\beta} \equiv (\hat{G})_{\alpha\beta}$. The non-interacting Green function is given by

$$\hat{G}^0(k) = \left[i\omega_n \mathbb{1} - (\hat{H}_0(\mathbf{k}) - \mu\mathbb{1}) \right]^{-1} , \tag{S21}$$

where H_0 is the non-interacting Hamiltonian given in Eq. (S11), $\mathbb{1}$ denotes the 2×2 identity matrix, and μ is the chemical potential of the doping level δ. The self-energy Σ mainly consists of contributions from spin and charge fluctuations and is calculated from

$$\Sigma_{\alpha\beta}(k) = \frac{T}{N_{\mathbf{k}}} \sum_q G_{\alpha\beta}(k-q) \left\{ U^2 \left[\frac{3}{2} \hat{\chi}^{\mathrm{s}}(q) + \frac{1}{2} \hat{\chi}^{\mathrm{c}}(q) - \hat{\chi}^0(q) \right] + \mathbb{1} U \right\}_{\alpha\beta} , \tag{S22}$$

with the number of sites $N_{\mathbf{k}}$, and the Hubbard interaction U as given in Eq. (2) of the main text. The charge and spin susceptibility entering Eq. (S22) are defined by

$$\hat{\chi}^{\mathrm{c,s}}(q) = \hat{\chi}^0(q) \left[\mathbb{1} \pm U \hat{\chi}^0(q) \right]^{-1} , \tag{S23}$$

where the irreducible susceptibility is

$$\chi^0_{\alpha\beta}(q) = -\frac{T}{N_{\mathbf{k}}} \sum_k G_{\alpha\beta}(k+q) G_{\beta\alpha}(k) . \tag{S24}$$

Eqs. (S20) – (S24) are solved self-consistently. The calculations are initialized using only the bare Green function G^0 with $\Sigma = 0$, i.e., starting from free electrons, and in each iteration step the chemical potential μ needs to be adjusted to keep the doping δ fixed. We employ a linear mixing $G = \kappa G^{\mathrm{new}} + (1-\kappa)G^{\mathrm{old}}$ with $\kappa = 0.2$. We then defined self-consistency for a relative difference of 10^{-4} between the self-energy of two iteration steps. In all calculations, we used a $\mathbf{k}$-mesh resolution of 120×120. For the Matsubara frequencies we used the sparse-sampling approach [S28–S30] of the intermediate representation (IR) basis [S31, S32] with an IR parameter $\Lambda = 10^4$ and a basis cutoff $\delta_{\mathrm{IR}} = 10^{-8}$. Since the numerical cost of FLEX calculations for $T = \mathcal{O}(0.001t)$ is quite expensive, this formalism is crucial. For instance, older works studying honeycomb models [S33–S35] could not determine the transition temperature T_{c}. Details on the implementation can be found in Ref. [S29] .

To study the superconducting phase transition driven by spin fluctuations, we consider the linearized gap equation

$$\lambda \Delta^S_{\alpha\beta}(k) = -\frac{T}{N_{\mathbf{k}}} \sum_q \sum_{\alpha',\beta'} V^S_{\alpha\beta}(q) G_{\alpha\alpha'}(k-q) G_{\beta\beta'}(q-k) \Delta^S_{\alpha'\beta'}(k-q) , \tag{S25}$$

for the pairing potential or gap function Δ on sublattice α and with spin orientation S. This equation represents an eigenvalue problem for Δ where the eigenvalue λ can be understood as the relative pairing strength of a certain pairing channel. The dominant pairing symmetry of the gap function has the largest eigenvalue λ and the transition temperature is found if λ reaches unity. Since we do not consider spin-orbit coupling, the linearized gap equation (S25) is diagonal in the spin singlet- and triplet-pairing channel ($S = 0, 1$) with the respective interactions due to the exchange of spin and charge fluctuations

$$\hat{V}^{S=0}(q) = \frac{3}{2} U^2 \hat{\chi}^{\mathrm{s}}(q) - \frac{1}{2} U^2 \hat{\chi}^{\mathrm{c}}(q) + \mathbb{1} U , \quad \hat{V}^{S=1}(q) = -\frac{1}{2} U^2 \hat{\chi}^{\mathrm{s}}(q) - \frac{1}{2} U^2 \hat{\chi}^{\mathrm{c}}(q) . \tag{S26}$$

We solve Eqs. (S25) and (S26) by using the power iteration method with a relative error of 10^{-4} for convergence. As an input serve the converged Green function of the normal state calculations and a trial gap function Δ_0, which is set up according to the irreducible representations of the D_6 symmetry group [S36].

S6. MAGNETIC QUASIORDER AND SPIN FLUCTUATIONS IN THE HONEYCOMB HUBBARD MODEL

In two dimensions, the Mermin-Wagner theorem [S37] prevents the formation of (genuine) long-range order at finite temperature as obeyed by the FLEX approximation [S38]. However, tendencies towards magnetic quasi-order can be read off from the Stoner enhancement factor $U\chi^0(\mathbf{q})$, which enters the denominator of the static spin susceptibility $\chi^{\mathrm{s}}(i\nu_0 = 0, \mathbf{q})$ (c.f. Eq. (S23)). Thus, possible formation of spin density waves (SDWs) can be investigated in FLEX by inspecting the instabilities of $\chi^{\mathrm{s}}(i\nu_0, \mathbf{q})$. When the Stoner enhancement approaches unity [$U\chi^0 \sim \mathcal{O}(0.99)$], χ^{s} diverges and the transition to a quasi-ordered magnetic state is assumed [S4, S39, S40]. At this point, the FLEX calculations turn unstable and do not converge anymore. A discussion of the leading Stoner enhancement, indicating regions of strong magnetic fluctuations, is given in the main text.

While the real-space profile of the magnetic fluctuations is discussed in the main text, Fig. 2(b), further insight into the emerging SDWs can be gained by inspecting the momentum-space structure of $\chi^{\mathrm{s}}(i\nu_0, \mathbf{q})$. In Fig. S6, we show the
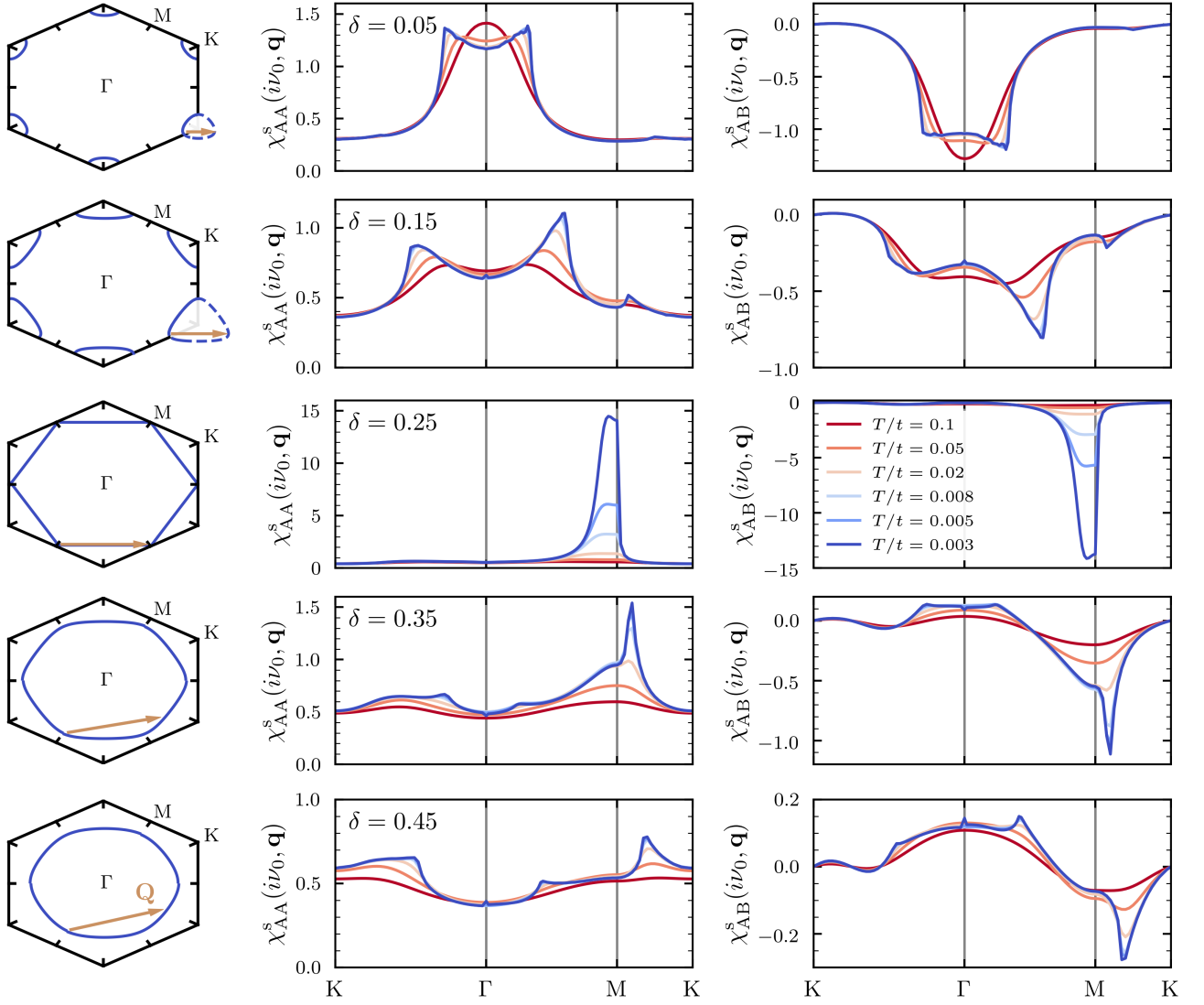
Figure S6. (Color online) Momentum dependent static spin susceptibility calculated in FLEX for different temperatures T/t and dopings δ (rows) at fixed interaction $U/t = 4$. The left column contains the non-interacting Fermi surfaces at the respective doping levels and the dominant nesting vectors $\mathbf{Q}$ associated with the largest peak of $\chi^s(i\nu_0, \mathbf{q})$. Middle and right column show the momentum resolved real part of the spin susceptibility within (AA-component) and between (AB-component) sublattices, respectively.

intra-sublattice (AA) and inter-sublattice (AB) components of $\chi^s(i\nu_0, \mathbf{q})$ along high-symmetry paths of the Brillouin zone for different δ and T at an intermediate interaction of $U/t = 4$. Additionally, we included the Fermi surfaces of the non-interacting system associated with each doping level.

In the doping range between the Dirac point and VHS, the AA- and AB-components of χ^s carry predominantly a different sign signaling antiferromagnetic fluctuations with respect to the A and B sublattices. Beyond the VHS, ferromagnetic fluctuations with respect to the sublattice index emerge and the relative fluctuation strength decreases. In each sublattice, the peak structure of χ^s changes significantly depending on the Fermi surface shape and becomes more pronounced for lower temperatures. That is, because the spin fluctuations emerge from the nesting conditions of the Fermi surface, i.e., possible intra-pocket electron scattering. To illustrate this, we also draw the nesting vector $\mathbf{Q}$ belonging to the dominant peak of χ^s between Fermi surface sheets.

Near Dirac doping ($\delta = 0.05$), the Fermi surface is formed by small, almost circular pockets around the K point so that long-wavelength SDWs emerge, since χ^s peaks close to the Γ point. This situation corresponds to an almost ferromagnetic ordering in each sublattice, but antiferromagnetic fluctuations between the sublattices. Increasing the doping ($\delta = 0.15$) deforms the Fermi surface to an equilateral shape whereby the spin fluctuations assume shorter wavelengths, as the peak in χ^s shifts from the Γ point to the M point. At the VHS ($\delta = 0.25$), the system undergoes
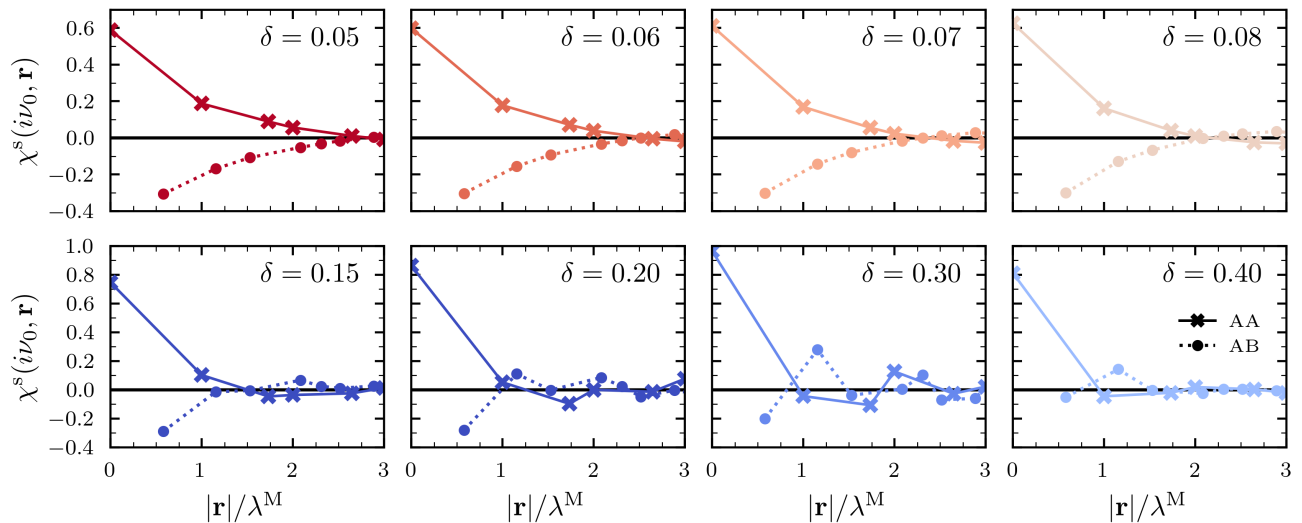
Figure S7. (Color online) Real space profile of the static spin susceptibility calculated in FLEX for different dopings δ at $T/t = 0.003$ and $U/t = 6$. The distance $|\mathbf{r}|$ of two lattice sites is given in units of the moiré length λ^{M}. Correlations between spins on equal (different) sublattice sites are marked by solid lines with crosses (dotted lines with circles), corresponding to the AA (AB) component of χ^{s}.

a Lifshitz transition and the Fermi surface turns hexagonal with perfect nesting conditions. This causes strong fluctuations with a chiral spin profile on each sublattice [S41, S42]. Beyond the VHS ($\delta = 0.35, 0.45$), the Fermi surface contracts around the Γ point with decreasing relative fluctuation strength. Increasing the interaction U enhances the fluctuation strength, but does not affect the general structure of χ^{s}.

Spin fluctuations can mediate an effective electron-electron interaction, as described by Eq. (S26). This interaction has non-local attractive regions which can pair spatially correlated electrons as they avoid occupying the same site. Thus, the real space profile $\chi^{\mathrm{s}}(i\nu_0, \mathbf{r})$ provides information on the pairing potential for electrons. In Fig. S7, we show $\chi^{\mathrm{s}}(i\nu_0, \mathbf{r})$ for different dopings at $T/t = 0.003$ and $U/t = 6$. In accordance with the previous discussion of the momentum space structure, antiferromagnetic correlations between different sublattice sites occur for doping levels in the vicinity of the Dirac point ($\delta \lesssim 0.15$) which turn ferromagnetic for larger dopings. By increasing the doping, the AA and AB components of χ^{s} change sign on a shorter length scale, so that regions with antiferromagnetic correlations shrink. This reduces the attractive regions ($V^S \sim \chi^{\mathrm{s}} < 0$) leading to a less optimal pairing situation since the pair electrons need to move closer while the Coulomb repulsion pushes them apart.

In the main text, we discuss that an optimal pairing condition with maximal transition temperature $T_{\mathrm{c}}^{\mathrm{max}}$ arises. This can be understood from the structure of $\chi^{\mathrm{s}}(i\nu_0, \mathbf{r})$ and DOS. Considering $U/t = 6$, $T_{\mathrm{c}}^{\mathrm{max}}$ is located around $\delta_{\mathrm{opt}} \sim 0.06 - 0.07$. The top row of Fig. S7 shows that the fourth- and fifth-nearest-neighbor component of $\chi_{\mathrm{AB}}^{\mathrm{s}}$ change sign in this doping region. Up to this point, T_{c} increases with doping driven by the increase in the DOS at the Fermi level (c.f. Fig. S1(c)). As the attractive region shrinks beyond δ_{opt}, pairing conditions deteriorate and T_{c} decreases. The optimal situation appears where these two counteracting trends are balanced.

S7. LEADING SUPERCONDUCTING INSTABILITY

The possible pairing symmetries of the superconducting order can be classified according to the irreducible representation of the point group symmetry of the system [S36]. The honeycomb lattice is of D_6 symmetry which can possibly host singlet extended s-wave, or degenerate d-wave ($d_{xy}, d_{x^2-y^2}$) as well as triplet degenerate p-wave (p_x, p_y), $f_{x(x^2-3y^2)}$-wave, or $f_{y(3x^2-y^2)}$-wave pairing. The dominant pairing symmetry emerges with the largest eigenvalue λ of the linearized gap equation (S25).

In Fig. S8(a), we compare λ of the d-wave and $f \equiv f_{x(x^2-3y^2)}$-wave pairing symmetry for different dopings δ between the Dirac point and VHS. These two parings emerge as the dominant pairing symmetries in the singlet and triplet pairing channel, respectively. The momentum dependence of the corresponding intra-sublattice order parameters at lowest Matsubara frequency $\Delta_{\mathrm{AA}}(i\omega_1, \mathbf{k})$ is shown in Fig. S8(b). By comparing the superconducting eigenvalues, it can be seen that singlet pairing is favored over triplet pairing. This is, in fact, consistent with the observed antiferromagnetic fluctuations as they support singlet pairing. Clearly, the d-wave pairing is the dominant
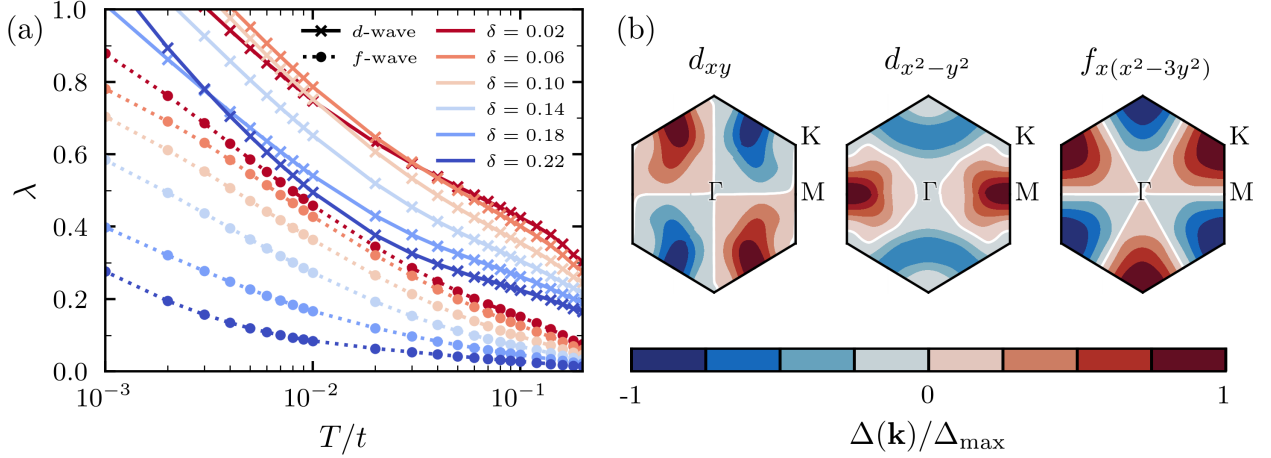
Figure S8. (Color online) Singlet vs. triplet superconductivity in the honeycomb Hubbard model. (a) Eigenvalues λ of the linearized Eliashberg equation for the degenerate d-wave (solid lines) and the $f \equiv f_{x(x^2-3y^2)}$-wave (dotted lines) pairing symmetries. Shown is the temperature dependence of λ for different dopings δ at $U/t = 6$. Note that the temperature scale is logarithmic. (b) Momentum-space structure of the order character for the d-wave and f-wave pairing symmetries. Shown are the normalized diagonal elements of the gap function Δ_{AA} at lowest Matsubara frequency for converged calculations at $T/t = 0.005$, $U/t = 6$, and $\delta = 0.1$. The nodes of the gap are indicated by white lines.

superconducting instability for which the critical temperature T_{c} is read off for $\lambda_d \to 1$. The values of λ_f, on the other hand, do not reach unity in the studied temperature region indicating that a possible transition would occur at considerably lower temperatures.

For the dominant d-wave pairing, we find that the pairing mainly takes place between different sublattices since we observe $|\Delta_{\mathrm{AB}}| > |\Delta_{\mathrm{AA}}|$. This is also in agreement with the antiferromagnetic alignment of the spins between the sublattices. Because of this, the triplet pairing instability can be enhanced and even dominate over the singlet pairing by introducing a staggered potential between the A and B sublattice sites [S33].

Below T_{c}, a linear combination of the degenerate d-wave states forms as the superconducting ground state. The exact realization depends on the free energy with the possibility of a chiral or nematic states [S36]. For the simple honeycomb lattice, the chiral $d+id$ state is the preferred solution with the lowest free energy [S43–S45], as the number of nodes in the quasiparticle spectrum is minimized in this case.

S8. INFLUENCE OF PARTICLE-HOLE ASYMMETRY ON SPIN-FLUCTUATION-MEDIATED SUPERCONDUCTIVITY

In Section S1, we discussed the influence of longer-ranged hopping terms on the band structure and DOS of the honeycomb lattice tight-binding model (c.f. Fig. S1(b) and (c)). Here, we assess the change of the spin-fluctuation-mediated superconducting phase transition line due to the resulting particle-hole asymmetry. We use the same parameters $t_2/t = -0.136$ and $t_3/t = 0.105$ as in Section S1. To describe the asymmetry, we need to compare each side of the Dirac point. We calculate the critical temperature $T_{\mathrm{c}}^{\mathrm{sp}}$ for one Hubbard parameter $U/t = 6$.

A comparison of the doping dependence of T_{c} for the particle-hole symmetric and asymmetric model is shown in Fig. S9. In accordance with the band structure and DOS asymmetry, an asymmetry in the doping dependence of $T_{\mathrm{c}}^{\mathrm{sp}}$ emerges. On the left side of the Dirac point, superconductivity is slightly enhanced, while it is suppressed on the other side. This might be contrary to expectations, since the enhancement/suppression of the DOS is opposite. The reason for this is a change in the shape of the Fermi surface and hence nesting conditions caused by the additional hopping terms. Near the Dirac point, the triangular parts of the Fermi surface become flatter and the spin fluctuation strength increases due to better nesting. At the VHS, the hexagonal shape of the Fermi surface becomes rounder causing weaker spin fluctuations. The extent to which this happens, is different for each side of the Dirac point resulting in two different curves. For instance, on the left side the DOS of both cases is similar, but $T_{\mathrm{c}}^{\mathrm{sp}}$ of the asymmetric model is slightly increased due to stronger spin fluctuations. The different nesting conditions also cause the VHS to be less detrimental to the calculations, since the Stoner enhancement does not diverge as strongly.

Even though quantitative aspects of $T_{\mathrm{c}}^{\mathrm{sp}}(\delta)$ change by the presence of long-range contributions to the single-particle
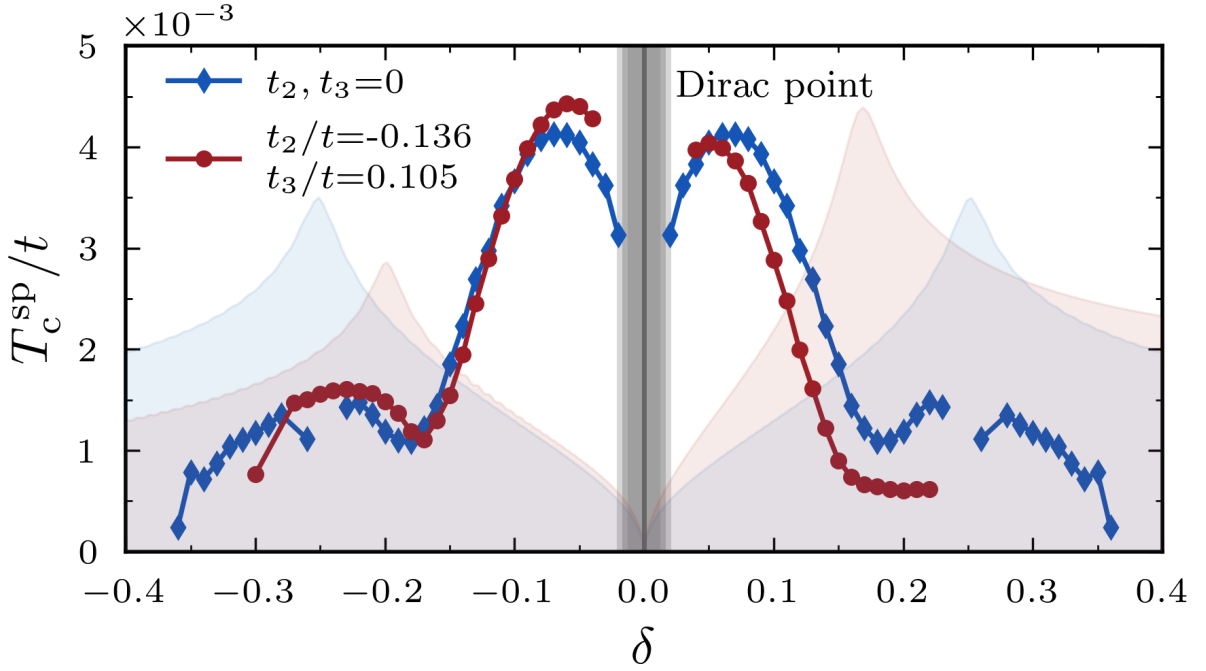
Figure S9. (Color online) Comparison of the doping dependence of the spin-fluctuation-driven superconducting transition line T_c^{sp} for the particle-hole symmetric ($t_2, t_3 = 0$, blue line with diamonds) and asymmetric ($t_2/t = -0.136$, $t_3/t = 0.105$, red line with circles) honeycomb lattice model. The density of states for each model is drawn by a shaded area to indicate the position of the Van Hove singularities (VHS) in each case and how the phononic transition line T_c^{ph} would differ qualitatively. The Dirac point and its vicinity are indicated by a gray shaded area.

dispersion, the general qualitative behavior remains unchanged. A clear maximum of T_c^{sp} exists on both sides of the Dirac point, while superconductivity is suppressed by doping away from that region. Still ferromagnetic fluctuations form beyond the VHS which lead to the absence of superconductivity.

S9. SUPERCONDUCTIVITY FROM NON-LOCAL ELECTRON-PHONON INTERACTION

In the main text, we have stated that conventional superconductivity driven by the electron–phonon interaction persists over a larger doping range and peaks at different levels than unconventional superconductivity driven by spin fluctuations. More precisely, using the approximations of a single Einstein phonon mode and a constant Holstein electron–phonon coupling, we have shown that the critical temperature closely follows the electronic DOS. Here, we will demonstrate that these observations remain valid for more general momentum-dependent phonon frequencies and Peierls electron–phonon coupling.

We describe the electrons and phonons of the moiré superlattice using nearest-neighbor-only tight-binding and mass–spring models on a honeycomb lattice. The tight-binding Hamiltonian is equivalent to the nearest-neighbor part of Eq. (S11), except that we change the orientation of the two electronic sublattices A, B and the primitive moiré lattice vectors $\mathbf{L}_{1,2}^{\mathrm{M}}$ for the sake of notational simplicity, see Fig. S10 (a). Using reciprocal lattice units $k_{1,2} = \mathbf{k} \cdot \mathbf{L}_{1,2}^{\mathrm{M}}$, the tight-binding Hamiltonian can then be defined as

$$H_{\mathbf{k}AB} = t(1 + \mathrm{e}^{ik_1} + \mathrm{e}^{-ik_2}), \quad H_{\mathbf{k}BA} = H_{\mathbf{k}AB}^*, \quad H_{\mathbf{k}AA} = H_{\mathbf{k}BB} = 0, \tag{S27}$$

where $t \equiv t_1$ and the asterisk denotes the complex conjugate. The corresponding electron dispersion relation (see Fig. S2 (b)) reads

$$E_{\mathbf{k}\pm} = \pm t\sqrt{3 + 2\cos(k_1) + 2\cos(k_2) + 2\cos(k_1 + k_2)}. \tag{S28}$$

For the phonons, we use a mass–spring model with an isotropic nearest-neighbor force constant. Using reciprocal lattice units $q_{1,2} = \mathbf{q} \cdot \mathbf{L}_{1,2}^{\mathrm{M}}$, the dynamical matrix can be defined as

$$D_{\mathbf{q}AB} = -\mathbb{1}\frac{k}{M}(1 + \mathrm{e}^{iq_1} + \mathrm{e}^{-iq_2}), \quad D_{\mathbf{q}BA} = D_{\mathbf{q}AB}^*, \quad D_{\mathbf{q}AA} = D_{\mathbf{q}BB} = \mathbb{1}\frac{3k}{M}, \tag{S29}$$

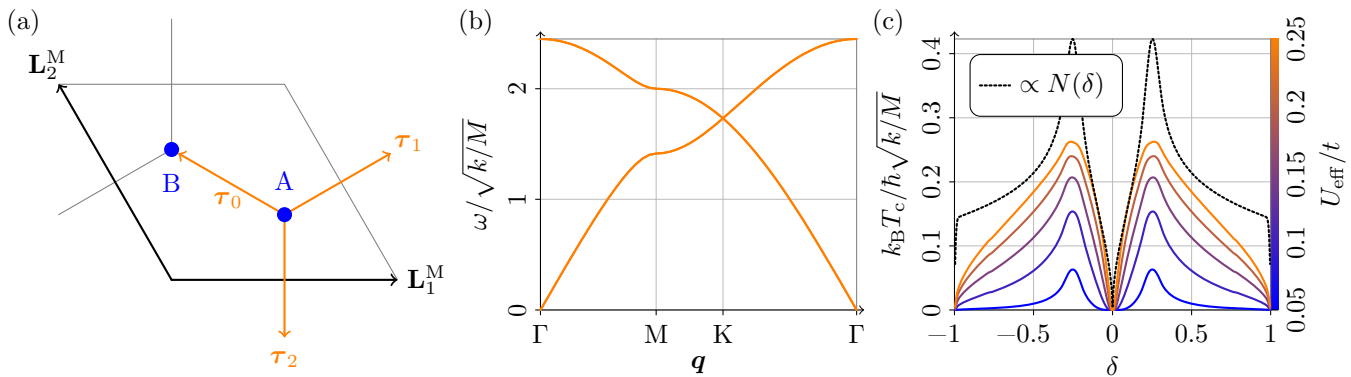Figure S10. (Color online) Non-local electron-phonon interactions. (a) Honeycomb lattice with primitive lattice vectors $\mathbf{L}^{\mathrm{M}}_{1,2}$, bond vectors $\tau_{0,1,2}$, and sublattices A, B. (b) Phonon dispersion $\omega_{\mathbf{q}\pm}$ in units of $\sqrt{k/M}$ with force constant k and mass M. (c) Critical temperature T_{c} in units of $\sqrt{k/M}$ and density of states N in arbitrary units as a function of the doping level δ for different strengths of the effective interaction U_{eff} in units of the hopping t.

where k and M are the effective force constant and a mass, respectively. The force constant and mass have to be understood as effective quantities related to the moiré unit cell and not referring to the primitive unit cell or individual atoms. $\mathbb{1}$ denotes the unit matrix in the space of Cartesian displacement directions.

We show in Fig. S10 (b) the corresponding phonon dispersion which consists of two branches, whose degeneracy is the number of spatial dimensions, and reads $\omega_{\mathbf{q}\pm} = \sqrt{k_{\mathbf{q}\pm}/M}$ with

$$k_{\mathbf{q}\pm} = k[3 \pm \sqrt{3 + 2\cos(q_1) + 2\cos(q_2) + 2\cos(q_1 + q_2)}]. \tag{S30}$$

Finally, modeling the dependence of the hopping t on the bond length τ as $t/t_0 = (\tau/\tau_0)^{-\beta}$ [S46] and labeling the sublattices of the ionic displacements as A′, B′, the deformation-potential matrix element can be defined as

$$\mathbf{d}_{\mathbf{q}\mathrm{A}'\mathbf{k}\mathrm{AB}} = \frac{\beta t}{\tau}(\hat{\tau}_0 + \hat{\tau}_1 \mathrm{e}^{\mathrm{i}k_1} + \hat{\tau}_2 \mathrm{e}^{-\mathrm{i}k_2}), \quad \mathbf{d}_{\mathbf{q}\mathrm{A}'\mathbf{k}\mathrm{BA}} = \mathbf{d}^*_{\mathbf{q}\mathrm{A}'\mathbf{k}+\mathbf{q}\mathrm{AB}}, \quad \mathbf{d}_{\mathbf{q}\mathrm{B}'\mathbf{k}ij} = -\mathbf{d}^*_{\mathbf{q}\mathrm{A}'\mathbf{k}ji}, \tag{S31}$$

where $\hat{\tau}_{0,1,2}$ are the normalized nearest-neighbor bond directions (Fig. S10 (a)) and $i, j \in \mathrm{A, B}$. $d_{\mathbf{q}x\mathbf{k}ij}$ quantifies the scattering of an electron from $\mathbf{k}, j$ to $\mathbf{k} + \mathbf{q}, i$ due to a $\mathbf{q}, x$ displacement. Using the eigenvectors ψ and $\mathbf{e}$ of the tight-binding Hamiltonian and the dynamical matrix, the deformation-potential matrix element can be transformed to the band basis via

$$d_{\mathbf{q}\nu\mathbf{k}mn} = \sum_{xij} e_{\mathbf{q}x\nu} \psi^*_{\mathbf{k}+\mathbf{q}im} \psi_{\mathbf{k}jn} d_{\mathbf{q}x\mathbf{k}ij}, \tag{S32}$$

where ν denotes the phonon branch and m, n the electronic band. The index x combines A′, B′ and Cartesian directions. With this, we have everything needed to calculate the effective electron–phonon coupling strength

$$\lambda(\mu) = N(\mu) \frac{\sum_{\mathbf{q}\nu\mathbf{k}mn} \delta(\epsilon_{\mathbf{k}+\mathbf{q}m} - \mu)\delta(\epsilon_{\mathbf{k}n} - \mu)U^{\mathrm{eff}}_{\mathbf{q}\nu\mathbf{k}mn}}{\sum_{\mathbf{q}\mathbf{k}mn} \delta(\epsilon_{\mathbf{k}+\mathbf{q}m} - \mu)\delta(\epsilon_{\mathbf{k}n} - \mu)}, \tag{S33}$$

where we have defined the effective attractive interaction $U^{\mathrm{eff}}_{\mathbf{q}\nu\mathbf{k}mn} = |d_{\mathbf{q}\nu\mathbf{k}mn}|^2/k_{\mathbf{q}\nu}$, and the logarithmic average of the phonon energy

$$\omega_{\log}(\mu) = \exp\left[\frac{\sum_{\mathbf{q}\nu\mathbf{k}mn} \delta(\epsilon_{\mathbf{k}+\mathbf{q}m} - \mu)\delta(\epsilon_{\mathbf{k}n} - \mu)U^{\mathrm{eff}}_{\mathbf{q}\nu\mathbf{k}mn} \log(\omega_{\mathbf{q}\nu})}{\sum_{\mathbf{q}\nu\mathbf{k}mn} \delta(\epsilon_{\mathbf{k}+\mathbf{q}m} - \mu)\delta(\epsilon_{\mathbf{k}n} - \mu)U^{\mathrm{eff}}_{\mathbf{q}\nu\mathbf{k}mn}}\right] \tag{S34}$$

as a function of the chemical potential μ [S47]. Here, $N(\mu)$ is the DOS per spin direction and unit cell, see Fig. S2(c) for the DOS as a function of the doping level δ. Both λ and $\omega_{\log}$ are double Fermi-surface averages; the δ functions ensure that both in- and outgoing states $\mathbf{k}, n$ and $\mathbf{k} + \mathbf{q}, m$ are on the Fermi surface. Note that the shape of λ and $\omega_{\log}$ as a function of μ for our model is fixed and their magnitude depends solely on the prefactors $U_{\mathrm{eff}}/t = \beta^2 t/\tau^2 k$ and $\sqrt{k/M}$, respectively.

We calculate the critical temperature T_c using McMillan's formula [S47, S48] (Eq. (3) of the main text) for different values of U_{eff} covering the entire range from weak to strong coupling, i.e., $0 < \lambda \lesssim 2$, as a function of the doping δ. For simplicity, we set the Coulomb pseudopotential $\mu^* = 0$, while finite μ^* do not change the picture qualitatively. We sample the Brillouin zone using $96 \times 96 \times 1$ **q** and **k** points in combination with a Gaussian broadening of $0.05t$. In all cases, T_c approximately follows the DOS, see Fig. S10 (c). Depending on the value of U_{eff}, the maxima at the VHS are more or less pronounced.

S10. ESTIMATION OF EFFECTIVE ELECTRON-PHONON INTERACTION PARAMETER U_{eff}

In the main text and in Section S9 we used McMillan's formula to show that superconductivity arising from electron-phonon coupling reveals generic and robust doping fingerprints by T_c following the DOS. The quantitative details of the superconducting transition are then determined by the material properties. Here, we give an estimation on the order of magnitude for the effective BCS-like interaction U_{eff} entering the pairing strength $\lambda = U_{\text{eff}} N(E_F)$ for Γ-valley twisted TMDCs.

The simplest estimation for the pairing strength λ for twisted moiré systems is to extrapolate from calculations for the untwisted material. In homobilayer TMDCs, λ can take values up to 8 [S49] depending on the doping with the DOS varying between $0.4\,\text{eV}^{-1}$ and $2\,\text{eV}^{-1}$ [S50]. Hence, the effective interaction strength is $U_{\text{eff}} = \lambda/N(E_F) \approx 4-12$ eV per unit cell. This value needs to be scaled to the moiré unit cell which contains approximately $(\lambda^M/a_0)^2 = 1/\sin^2\theta \approx \theta^{-2}$ single unit cells with lattice constant a_0 (c.f. Table S1) for small θ, i.e., the effective interaction is twist-angle dependent $U_{\text{eff}}(\theta) \approx 4-12\,\theta^2$ eV. Using our observation $t \propto \theta^2$ (c.f. Fig. 1(c) of the main text), we can express U_{eff} in units of t. For instance, for twisted MoS$_2$ bilayer we can write $t \approx 2$ eV$\cdot\theta^2 = \alpha\theta^2$ with θ in radians. Thus, we estimate an interaction strength of $U_{\text{eff}}/t = 2-6$.

We also discuss moiré phonon modes, where we obtain $U_{\text{eff}} = d^2/k$ from elastic properties of the bilayer TMDCs. Instead of using the microsopic electron-phonon coupling g and the averaged ("typical") phonon frequency $\langle\omega\rangle$, we express U_{eff} in terms of an effective moiré deformation potential d and an effective moiré force constant k. They are related by

$$U_{\text{eff}} = \frac{2g^2}{\hbar\langle\omega\rangle} = \frac{2}{\hbar\langle\omega\rangle}\frac{\hbar d^2}{2M\langle\omega\rangle} = \frac{d^2}{k} \, , \tag{S35}$$

since $g = \sqrt{\frac{\hbar}{2M\langle\omega\rangle}}d$ [S51] and $\langle\omega\rangle = \sqrt{k/M}$ with mass M. It shows that the attractive phonon-mediated interaction can be interpreted as a classical quantity, as all $\hbar$ cancel out.

First, we consider a case which corresponds to a purely local mode with Holstein-type coupling, which results from an interlayer breathing mode, see Fig. S11(a). In this case, a restoring force $F = k\Delta h$ is induced when the interlayer distance is changed by an amount Δh. The response of the system is also encoded in the elastic constant in out-of-plane direction

$$C_{33} = \frac{\sigma}{\varepsilon} = \frac{F/A}{\Delta h/h} = \frac{Fh}{A\Delta h} \tag{S36}$$

with the tensile stress σ of the lifted area A and strain ε of the equilibrium layer distance h. Thus, the force constant can be calculated from

$$k = \frac{F}{\Delta h} = \frac{A\,C_{33}}{h} \, . \tag{S37}$$

We assume that only a fraction $p < 1$ (the AB, BA regions) of the moiré unit cell needs to be lifted, so that $A = p\frac{\sqrt{3}}{2}(\lambda^M)^2 \approx p\frac{\sqrt{3}}{2}a_0^2\theta^{-2}$. The magnitude of the deformation potential is given in Eq. (S31) and for a single mode it simplifies to

$$d = \frac{\beta t_\perp}{h} \tag{S38}$$

with the interlayer hopping $t_\perp$. The attractive interaction in Eq. (S35) then takes the form

$$U_{\text{eff}}^{\text{Holst.}} = \frac{d^2}{k} = \left(\frac{\beta t_\perp}{h}\right)^2 \cdot \frac{h}{A\,C_{33}} \approx \frac{\beta^2 t_\perp^2}{\frac{\sqrt{3}}{2}pa_0^2\theta^{-2}hC_{33}} \, . \tag{S39}$$
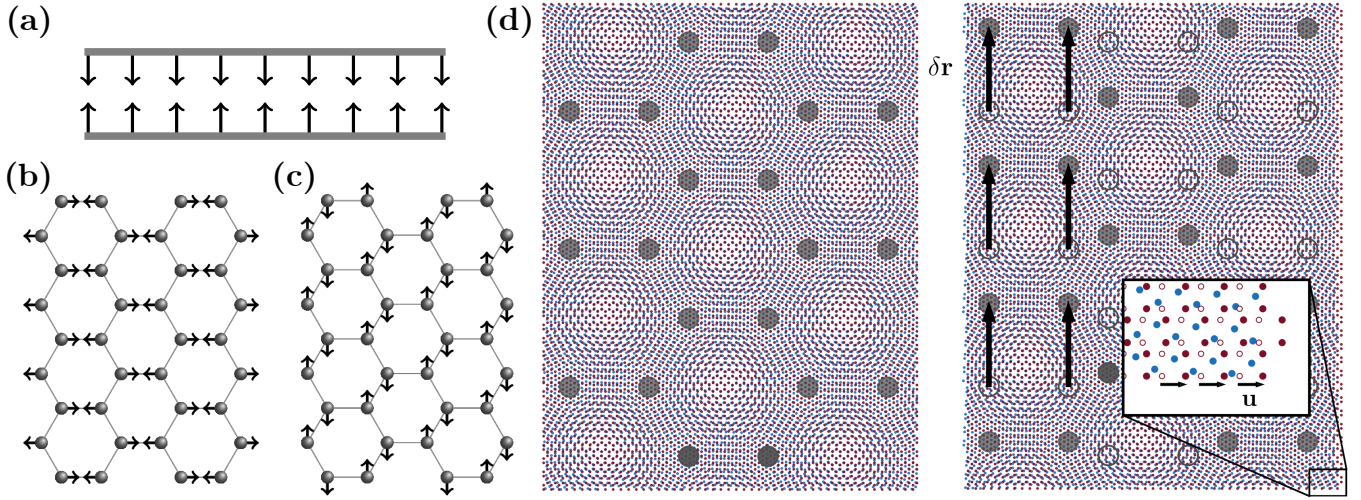
Figure S11. (Color online) Moiré phonon modes. (a) Layer-breathing mode ("Holstein" coupling). (b,c) Optical in-plane modes of a honeycomb lattice at Γ ("Peierls" coupling). (d) Effect of TMDC layer displacement. The left panel shows the unshifted lattice, while in the right panel the red TMDC lattice was displaced to the right by $\mathbf{u}$, so that the moiré superlattice is shifted to the top by $\delta\mathbf{r}$. Empty circles denote the unshifted atom positions.

Expressing $U_{\text{eff}}^{\text{Holst.}}$ in units of the moiré honeycomblattice hopping $t \approx \alpha\theta^2$ yields

$$U_{\text{eff}}^{\text{Holst.}} \approx \frac{2}{\sqrt{3}} \frac{\beta^2 t_\perp^2}{\alpha p a_0^2 h C_{33}} t \, . \tag{S40}$$

We can estimate $U_{\text{eff}}^{\text{Holst.}}$ to be in the range of $0.05-1.4\,t$ by assuming $\beta = 4-5$ [S46], $a_0 = 3.18$ Å[S50], $C_{33} = 52$ GPa [S52, S53], $t_\perp = 0.3-0.4$ eV [S1], $h = 3-6$ Å, $\alpha = 2$ eV, and $p = 0.167-0.5$. In our simplified approach, we thus get interactions that can induce superconductivity (c.f. Fig. S3(b) of the main text) since the pairing strength $\lambda = U_{\text{eff}}/t \cdot N(E_{\text{F}})t$ reaches values up to $\lambda \approx 0.5$ (c.f. Fig. S2(c)).

Now, we consider an interlayer shear mode with the two layers being moved in opposite directions and opposite shearing profile in the AB and BA regions of the moiré. This effectively modulates the bond lengths in the moiré honeycomb superlattice, i.e., we estimate the effective interaction arising from the Peierls coupling discussed in Section S9. Two equivalent shear modes exist, see Fig. S11(b,c), for which the potential energy is given by the optical $\mathbf{q} = \mathbf{0}$ eigenmode (c.f. Eq. (S30)) of the spring model in Section S9. The displacement δr_0 of a Wannier center with respect to the origin at an AB/BA site thus has the elastic energy

$$E_{\text{el}} = \frac{1}{2} k_{\mathbf{q}=\mathbf{0},+} \delta r_0^2 = 3k\,\delta r_0^2 \, . \tag{S41}$$

On the other hand, we can estimate the equivalent displacement energy [S54]

$$E = \frac{1}{2} \int_{A_{\text{M}}} d^2 r \, \sum_\alpha \lambda_{\text{L}} u_{\alpha\alpha}^2 + \sum_{\alpha\beta} 2\mu_{\text{L}} u_{\alpha\beta}^2 \tag{S42}$$

associated with the displacement field $\mathbf{u}$ of a single layer. Here, $u_{\alpha\beta} = \frac{1}{2}(\frac{\partial u_\alpha}{\partial x_\beta} + \frac{\partial u_\beta}{\partial x_\alpha} + \sum_\gamma \frac{\partial u_\gamma}{\partial x_\alpha} \frac{\partial u_\gamma}{\partial x_\beta})$ is the strain tensor and $\lambda_{\text{L}}, \mu_{\text{L}}$ are the Lamé constants which are linked to the Young's modulus Y and Poisson ratio ν via

$$\lambda_{\text{L}} = \frac{\nu}{1-2\nu}\frac{1}{1+\nu}Y \, , \quad \mu_{\text{L}} = \frac{1}{2(1+\nu)}Y \tag{S43}$$

with $Y \approx 150$ N/m and $\nu \approx 0.22$ for TMDC homobilayers [S55, S56]. The shear displacement $\mathbf{u}$ of the TMDC layers induces a perpendicular shift $\delta\mathbf{r}$ of the Wannier center with respect to the origin at an AB site as shown Fig. S11(d). They are linked by

$$\mathbf{u}_\pm = \left[\mathcal{R}_{\pm\theta/2} - \mathbb{1}_{2\times2}\right]\delta\mathbf{r} \approx \begin{pmatrix} 0 & \pm\frac{\theta}{2} \\ \mp\frac{\theta}{2} & 0 \end{pmatrix}\delta\mathbf{r} \, , \tag{S44}$$

for small twist angles where the upper and lower TMDC layer carry a different sign. For each mode the displacement field $\delta\mathbf{r}_{(b,c)} = \delta r(\mathbf{r})\mathbf{e}_{x,y}$ can be described by the leading Fourier components

$$\delta r(\mathbf{r}) = \frac{2\delta r_0}{3\sqrt{3}} \left(\sin(\mathbf{G}_1^{\mathrm{M}}\mathbf{r}) + \sin([\mathbf{G}_2^{\mathrm{M}} - \mathbf{G}_1^{\mathrm{M}}]\mathbf{r}) - \sin(\mathbf{G}_2^{\mathrm{M}}\mathbf{r})\right) \ . \tag{S45}$$

Since the shear modes (and displacement energies) are equivalent, we focus on the mode in Fig. S11(b) in the following. For this mode, we have the stress tensor components

$$
\begin{aligned}
u_{xx} &= 0 \ , \\
u_{xy} = u_{yx} &= \frac{1}{2}\frac{\partial u_y}{\partial x} = \pm\frac{\theta\delta r_0}{12}G^{\mathrm{M}}\left(\cos(\mathbf{G}_1^{\mathrm{M}}\mathbf{r}) + \cos([\mathbf{G}_2^{\mathrm{M}} - \mathbf{G}_1^{\mathrm{M}}]\mathbf{r})\right) \ , \\
u_{yy} &= \frac{\partial u_y}{\partial y} = \pm\frac{\theta\delta r_0}{6\sqrt{3}}G^{\mathrm{M}}\left(\cos(\mathbf{G}_1^{\mathrm{M}}\mathbf{r}) + \cos([\mathbf{G}_2^{\mathrm{M}} - \mathbf{G}_1^{\mathrm{M}}]\mathbf{r}) - 2\cos(\mathbf{G}_2^{\mathrm{M}}\mathbf{r}))\right)
\end{aligned}
\tag{S46}
$$

where the higher order terms of the offdiagonal components were neglected for small displacements and $G^{\mathrm{M}} = |\mathbf{G}_{1,2}^{\mathrm{M}}| = 2\pi/\lambda^{\mathrm{M}}$. Inserting Eq. (S46) into Eq. (S42) and integrating over the moiré unit cell area, the displacement energy for one layer yields

$$E = \frac{1}{2}\frac{\theta^2\delta r_0^2}{36}(G^{\mathrm{M}})^2 A_{\mathrm{M}}(\lambda_{\mathrm{L}} + 3\mu_{\mathrm{L}}) \ . \tag{S47}$$

We obtain the force constant by equating the displacement energy for both layers with twice (due to two layers) the elastic energy in Eq. (S41) and using Eq. (S43) as

$$k = \frac{2}{3\delta r_0^2}E_{\mathrm{el}} = \frac{1}{108}(G^{\mathrm{M}})^2 A_{\mathrm{M}}(\lambda_{\mathrm{L}} + 3\mu_{\mathrm{L}})\theta^2 = \frac{\sqrt{3}\pi^2}{108}\frac{3 - 4\nu}{(1 - 2\nu)(1 + \nu)}Y\theta^2 = k_0\theta^2 \tag{S48}$$

with $k_0 \approx 5.6$ eV/$\mathrm{\AA}^2$. The deformation potential is as in Eq. (S38) with $t_\perp$ and h being replaced by t and $\lambda^{\mathrm{M}}/3$ (Wannier orbital extent), respectively. The effective potential takes the form

$$U_{\mathrm{eff}}^{\mathrm{Peierls}} \approx \frac{\left(\beta t\frac{3}{\lambda^{\mathrm{M}}}\right)^2}{k_0\theta^2} \approx \frac{9\beta^2 t^2\left(\frac{\theta}{a_0}\right)^2}{k_0\theta^2} = \frac{9\beta^2}{a_0^2 k_0}t^2 = \frac{9\alpha\beta^2}{a_0^2 k_0}\theta^2 \cdot t \ . \tag{S49}$$

Since $U_{\mathrm{eff}}^{\mathrm{Peierls}}/t \propto t \propto \theta^2$ with the prefactor $\frac{9\alpha\beta^2}{a_0^2 k_0} \approx 5\text{--}8$, the effective interaction and hence pairing strength is very small. From our estimation we conclude that superconductivity from moiré Peierls coupling will not be realized in the real material system.

[S1] M. Angeli and A. H. MacDonald, Γ valley transition metal dichalcogenide moiré bands, Proc. Natl. Acad. Sci. **118**, e2021826118 (2021), arXiv:2008.01735.

[S2] T. Cea, N. R. Walet, and F. Guinea, Electronic band structure and pinning of Fermi energy to Van Hove singularities in twisted bilayer graphene: A self-consistent approach, Phys. Rev. B **100**, 205113 (2019).

[S3] T. Cea and F. Guinea, Band structure and insulating states driven by Coulomb interaction in twisted bilayer graphene, Phys. Rev. B **102**, 045107 (2020).

[S4] N. E. Bickers, D. J. Scalapino, and S. R. White, Conserving Approximations for Strongly Correlated Electron Systems: Bethe-Salpeter Equation and Dynamics for the Two-Dimensional Hubbard Model, Phys. Rev. Lett. **62**, 961 (1989).

[S5] N. E. Bickers and D. J. Scalapino, Conserving approximations for strongly fluctuating electron systems. I. Formalism and calculational approach, Ann. Phys. (NY) **193**, 206 (1989).

[S6] D. Xiao, G.-B. Liu, W. Feng, X. Xu, and W. Yao, Coupled Spin and Valley Physics in Monolayers of MoS$_2$ and Other Group-VI Dichalcogenides, Phys. Rev. Lett. **108**, 196802 (2012).

[S7] S. Venkateswarlu, A. Honecker, and G. Trambly de Laissardière, Electronic localization in twisted bilayer mos$_2$ with small rotation angle, Phys. Rev. B **102**, 081103 (2020).

[S8] N. Marzari, A. A. Mostofi, J. R. Yates, I. Souza, and D. Vanderbilt, Maximally localized Wannier functions: Theory and applications, Rev. Mod. Phys. **84**, 1419 (2012).

[S9] N. F. Q. Yuan, H. Isobe, and L. Fu, Magic of high-order van Hove singularity, Nat Commun. **10**, 5769 (2019).

[S10] L. Classen, A. V. Chubukov, C. Honerkamp, and M. M. Scherer, Competing orders at higher-order Van Hove points, Phys. Rev. B **102**, 125141 (2020).

[S11] F. Guinea and N. R. Walet, Electrostatic effects, band distortions, and superconductivity in twisted graphene bilayers, Proc. Natl. Acad. Sci. **115**, 13174 (2018).

[S12] M. J. Calderón and E. Bascones, Interactions in the 8-orbital model for twisted bilayer graphene, Phys. Rev. B **102**, 155149 (2020).

[S13] A. Fischer, Z. A. H. Goodwin, A. A. Mostofi, J. Lischner, D. M. Kennes, and L. Klebl, Unconventional superconductivity in magic-angle twisted trilayer graphene, npj Quantum Mater. **7**, 5 (2022).

[S14] G. P. Kerker, Efficient iteration scheme for self-consistent pseudopotential calculations, Phys. Rev. B **23**, 3082 (1981).

[S15] E. G. C. P. van Loon, M. Schüler, M. I. Katsnelson, and T. O. Wehling, Capturing nonlocal interaction effects in the Hubbard model: Optimal mappings and limits of applicability, Phys. Rev. B **94**, 165141 (2016).

[S16] J. M. Pizarro, M. Rösner, R. Thomale, R. Valentí, and T. O. Wehling, Internal screening and dielectric engineering in magic-angle twisted bilayer graphene, Phys. Rev. B **100**, 161102 (2019).

[S17] K. Ohno, Some remarks on the Pariser-Parr-Pople method, Theoretica chimica acta **2**, 219 (1964).

[S18] T. Cea and F. Guinea, Coulomb interaction, phonons, and superconductivity in twisted bilayer graphene, Proc. Natl. Acad. Sci. **118**, e2107874118 (2021).

[S19] A. Laturia, M. L. Van de Put, and W. G. Vandenberghe, Dielectric properties of hexagonal boron nitride and transition metal dichalcogenides: from monolayer to bulk, npj 2D Mater. Appl. **2**, 6 (2018).

[S20] A. Weston, Y. Zou, V. Enaldiev, A. Summerfield, N. Clark, V. Zólyomi, A. Graham, C. Yelgel, S. Magorrian, M. Zhou, J. Zultak, D. Hopkinson, A. Barinov, T. H. Bointon, A. Kretinin, N. R. Wilson, P. H. Beton, V. I. Fal'ko, S. J. Haigh, and R. Gorbachev, Atomic reconstruction in twisted bilayers of transition metal dichalcogenides, Nat. Nanotechnol. **15**, 592 (2020).

[S21] Z. A. H. Goodwin, F. Corsetti, A. A. Mostofi, and J. Lischner, Twist-angle sensitivity of electron correlations in moiré graphene bilayers, Phys. Rev. B **100**, 121106 (2019).

[S22] P. Stepanov, I. Das, X. Lu, A. Fahimniya, K. Watanabe, T. Taniguchi, F. H. L. Koppens, J. Lischner, L. Levitov, and D. K. Efetov, Untying the insulating and superconducting orders in magic-angle graphene, Nature **583**, 375 (2020).

[S23] Y. Saito, J. Ge, K. Watanabe, T. Taniguchi, and A. F. Young, Independent superconductors and correlated insulators in twisted bilayer graphene, Nat. Phys. **16**, 926 (2020).

[S24] H. S. Arora, R. Polski, Y. Zhang, A. Thomson, Y. Choi, H. Kim, Z. Lin, I. Z. Wilson, X. Xu, J.-H. Chu, K. Watanabe, T. Taniguchi, J. Alicea, and S. Nadj-Perge, Superconductivity in metallic twisted bilayer graphene stabilized by WSe_2, Nature **583**, 379 (2020).

[S25] X. Liu, Z. Wang, K. Watanabe, T. Taniguchi, O. Vafek, and J. I. A. Li, Tuning electron correlation in magic-angle twisted bilayer graphene using Coulomb screening, Science **371**, 1261 (2021).

[S26] H. Kontani and K. Ueda, Electronic Properties of the Trellis-Lattice Hubbard Model: Pseudogap and Superconductivity, Phys. Rev. Lett. **80**, 5619 (1998).

[S27] S. Koikegami, S. Fujimoto, and K. Yamada, Electronic Structure and Transition Temperature of the d-p Model, J. Phys. Soc. Jpn. **66**, 1438 (1997).

[S28] J. Li, M. Wallerberger, N. Chikano, C.-N. Yeh, E. Gull, and H. Shinaoka, Sparse sampling approach to efficient ab initio calculations at finite temperature, Phys. Rev. B **101**, 035144 (2020), arxiv:1908.07575.

[S29] N. Witt, E. G. C. P. van Loon, T. Nomoto, R. Arita, and T. O. Wehling, Efficient fluctuation-exchange approach to low-temperature spin fluctuations and superconductivity: From the Hubbard model to $Na_xCoO_2 \cdot yH_2O$, Phys. Rev. B **103**, 205148 (2021), arXiv:2012.04562.

[S30] H. Shinaoka, N. Chikano, E. Gull, J. Li, T. Nomoto, J. Otsuki, M. Wallerberger, T. Wang, and K. Yoshimi, Efficient ab initio many-body calculations based on sparse modeling of Matsubara Green's function, 2106.12685.

[S31] H. Shinaoka, J. Otsuki, M. Ohzeki, and K. Yoshimi, Compressing Green's function using intermediate representation between imaginary-time and real-frequency domains, Phys. Rev. B **96**, 035147 (2017), arxiv:1702.03054.

[S32] N. Chikano, K. Yoshimi, J. Otsuki, and H. Shinaoka, irbasis: Open-source database and software for intermediate-representation basis functions of imaginary-time Green's function, Comput. Phys. Commun. **240**, 181 (2019), arXiv:1807.05237.

[S33] K. Kuroki and R. Arita, Spin-triplet superconductivity in repulsive Hubbard models with disconnected Fermi surfaces: A case study on triangular and honeycomb lattices, Phys. Rev. B **63**, 174507 (2001).

[S34] S. Onari, K. Kuroki, R. Arita, and H. Aoki, Superconductivity induced by interband nesting in the three-dimensional honeycomb lattice, Phys. Rev. B **65**, 184525 (2002).

[S35] K. Kuroki, Spin-fluctuation-mediated $d+id'$ pairing mechanism in doped β-MNCl(M=Hf,Zr)superconductors, Phys. Rev. B **81**, 104502 (2010).

[S36] M. Sigrist and K. Ueda, Phenomenological theory of unconventional superconductivity, Rev. Mod. Phys. **63**, 239 (1991).

[S37] N. D. Mermin and H. Wagner, Absence of Ferromagnetism or Antiferromagnetism in One- or Two-Dimensional Isotropic Heisenberg Models, Phys. Rev. Lett. **17**, 1307 (1966).

[S38] H. Kontani and M. Ohno, Effect of a nonmagnetic impurity in a nearly antiferromagnetic Fermi liquid: Magnetic correlations and transport phenomena, Phys. Rev. B **74**, 014406 (2006).

[S39] H. Kino and H. Kontani, Phase Diagram of Superconductivity on the Anisotropic Triangular Lattice Hubbard Model: An Effective Model of κ-(BEDT-TTF) Salts, J. Phys. Soc. Jpn. **67**, 3691 (1998), arxiv:cond-mat/9807147.

[S40] M. Kitatani, N. Tsuji, and H. Aoki, FLEX+DMFT approach to the d-wave superconducting phase diagram of the two-dimensional Hubbard model, Phys. Rev. B **92**, 085104 (2015), arXiv:1505.04865.

[S41] W.-S. Wang, Y.-Y. Xiang, Q.-H. Wang, F. Wang, F. Yang, and D.-H. Lee, Functional renormalization group and variational Monte Carlo studies of the electronic instabilities in graphene near $\frac{1}{4}$ doping, Phys. Rev. B **85**, 035414 (2012).

[S42] S. Jiang, A. Mesaros, and Y. Ran, Chiral Spin-Density Wave, Spin-Charge-Chern Liquid, and $d + id$ Superconductivity in 1/4-Doped Correlated Electronic Systems on the Honeycomb Lattice, Phys. Rev. X **4**, 031040 (2014).

[S43] Z. Kuznetsova and V. Barzykin, Pairing state in multicomponent superconductors, Europhys. Lett. **72**, 437 (2005).

[S44] R. Nandkishore, L. S. Levitov, and A. V. Chubukov, Chiral superconductivity from repulsive interactions in doped graphene, Nat. Phys. **8**, 158 (2012).

[S45] A. M. Black-Schaffer and C. Honerkamp, Chiral d-wave superconductivity in doped graphene, J. Phys.: Condens. Matter **26**, 423201 (2014), arxiv:1406.0101.

[S46] W. A. Harrison, *Elementary Electronic Structure*, rev. ed. (World Scientific, Singapore, 2004).

[S47] P. B. Allen and R. C. Dynes, Transition temperature of strong-coupled superconductors reanalyzed, Phys. Rev. B **12**, 905 (1975).

[S48] W. L. McMillan, Transition Temperature of Strong-Coupled Superconductors, Phys. Rev. **167**, 331 (1968).

[S49] M. Rösner, S. Haas, and T. O. Wehling, Phase diagram of electron-doped dichalcogenides, Phys. Rev. B **90**, 245105 (2014).

[S50] G. Schönhoff, M. Rösner, R. E. Groenewald, S. Haas, and T. O. Wehling, Interplay of screening and superconductivity in low-dimensional materials, Phys. Rev. B **94**, 134504 (2016).

[S51] G. D. Mahan, *Many-Particle Physics*, 3rd ed. (Springer US, 2000).

[S52] J. L. Feldman, Elastic constants of 2H-MoS_2 and 2H-$NbSe_2$ extracted from measured dispersion curves and linear compressibilities, J. Phys. Chem. Solids **37**, 1141 (1976).

[S53] Y. Zhao, X. Luo, H. Li, J. Zhang, P. T. Araujo, C. K. Gan, J. Wu, H. Zhang, S. Y. Quek, M. S. Dresselhaus, and Q. Xiong, Interlayer Breathing and Shear Modes in Few-Trilayer MoS_2 and WSe_2, Nano Lett. **13**, 1007 (2013).

[S54] L. D. Landau and E. M. Lifshitz, *Theory of Elasticity*, 2nd ed., Vol. 7 (Oxford: Pergamon, 1970).

[S55] D. Çakır, F. M. Peeters, and C. Sevik, Mechanical and thermal properties of h-MX_2 (M=Cr, Mo, W; X=O, S, Se, Te) monolayers: A comparative study, Appl. Phys. Lett. **104**, 203110 (2014).

[S56] K. Liu, Q. Yan, M. Chen, W. Fan, Y. Sun, J. Suh, D. Fu, S. Lee, J. Zhou, S. Tongay, J. Ji, J. B. Neaton, and J. Wu, Elastic Properties of Chemical-Vapor-Deposited Monolayer MoS_2, WS_2, and Their Bilayer Heterostructures, Nano Lett. **14**, 5097 (2014).